Journal of Petroleum Science and Engineering 217 (2022) 110849

Contents lists available at ScienceDirect

Journal of Petroleum Science and Engineering

journal homepage: www.elsevier.com/locate/petrol

New method of in situ high-resolution experiments and analysis of fracture networks formed by hydraulic fracturing

Siping Zheng [a,b], Mian Lin [a,b,*], Wenbin Jiang [a,b], Xin Qiu [a,b], Zhuo Chen [a,b]

[a] Institute of Mechanics, Chinese Academy of Sciences, Beijing, 100190, China
[b] School of Engineering Science, University of Chinese Academy of Sciences, Beijing, 100049, China

ARTICLE INFO

Keywords:
Hydraulic fracturing
In situ
High-resolution
Tight sandstone
Fracture networks

ABSTRACT

Hydraulic fracturing plays a key role in the oil and gas development of unconventional tight reservoirs. Therefore, it is important to study the fracturing mechanism of rocks. Thus far, the exploration of this problem through laboratory experiments has been regarded as the best method. However, the current laboratory experiments cannot achieve in situ high-resolution observation and analysis. Accordingly, an online scanning platform composed of hydraulic fracturing and micro-computed tomography (HFCP) was developed in this study. The in situ measurements obtained using the HFCP include three parts: a computed tomography (CT) system with a maximum imaging resolution of 7 μm, a power system with a continuous changeable fluid pressure, and a post-processing system with rock reconstruction, grayscale calibration, threshold segmentation and efficient extraction of the fracture network. Furthermore, we carried out hydraulic fracturing experiments on tight sandstone samples using the HFCP, and the entire experimental process was conducted in situ. The statistics showed that under different confining pressures, the breakdown pressure and average fracture aperture increased with increasing injection rate, but the branch fracture volume fraction exhibited diverse characteristics. The HFCP provides a new method of studying the mechanism of the hydraulic fracturing of rocks, and it has the potential to reveal the in situ differences in fracture networks in tight reservoirs.

1. Introduction

As the main method of stimulating oil and gas production, hydraulic fracturing plays a key role in the oil and gas development of unconventional and tight reservoirs (Zhou et al., 2019; Li et al., 2019; Wu et al., 2021). Because it is difficult to observe and directly measure the fracture network in a reservoir during hydraulic fracturing, laboratory experiments and numerical simulations have become important methods in hydraulic fracturing research (Feng et al., 2019; Roth et al., 2020). For a long time, laboratory experiments have been the most direct and reliable method for determining the micro-characteristics of fractures in rocks and reservoirs. Laboratory experiments are also a powerful tool for verifying the effectiveness of numerical simulation results (Hampton et al., 2018; Li and Shi, 2021). Therefore, in recent years the focus of such research has remained achieving the direct observation and statistical analysis of laboratory hydraulic fracturing (Qian et al., 2020; Chen et al., 2020).

The fracture network is one of the main indicators for evaluating the effect of hydraulic fracturing. Therefore, many researchers have conducted a variety of fracturing experiments to study the influences of various factors on the formation of the fracture network. The shale fracturing experiments conducted by Lin et al. (2016) revealed that the fracture network induces complex morphologies when the fractures encounter bedding planes with weaker cementation. Deng et al. (2018) found that the propagation of inclined fractures perpendicular to the minimum principal stress was limited by the shear stress. The confining pressure around the rock was simulated by Zhang et al. (2019) in fracturing experiments, and they demonstrated that the shape of fractures became simpler as the stress difference increases. Large-scale tight sandstone experiments were carried out by Guo et al. (2021), and it was found that a high injection rate increased the longitudinal expansion range of the fractures. The above-mentioned fracture studies were mainly conducted on the millimeter or larger scales. However, because oil and gas production usually includes multiple stages from matrix pores to millimeter-scale fractures, studying the smaller-scale complex microfracture network is also important. Based on the studies of Du et al. (2020) and Gou et al. (2021) the morphology and distribution of the complex microfracture network formed during the fracturing process

* Corresponding author. Institute of Mechanics, Chinese Academy of Sciences, Beijing, 100190, China.
E-mail address: linmian@imech.ac.cn (M. Lin).

https://doi.org/10.1016/j.petrol.2022.110849
Received 15 February 2022; Received in revised form 30 May 2022; Accepted 4 July 2022
Available online 7 July 2022

can significantly improve the fracturing effect.

With the rapid development of high-resolution equipment, the growth mode of microfractures in rocks has been described by many researchers using micro-computed tomography (micro-CT) or scanning electron microscopy (SEM). Based on micro-CT observations, Jiang et al. (2019) determined that the complexity and extension distance of fractures plays an important role in the change in the shale fracturing volume. He et al. (2020) calculated the length of the microfractures in the hydraulic fracture network using SEM, and the results usually exhibited a lognormal distribution. The influence of temperature on the growth of hydraulic fracture network was discussed by Li et al. (2021) . They proved that the average value of the microfracture tortuosity increases as the temperature gradually increases. Yang et al. (2021) compared the effects of different fracturing fluids on the complexity of fracture network and determined that the volume fraction of fracture network produced by SC-CO_2 is 4.4 times that produced by water. The above-mentioned studies used high-resolution equipment to summarize the various laws of rock microfracture growth after fracturing. Unfortunately, these experiments required to unload the rock samples before observing the fractures. The gradual loss of fluid pressure during the unloading led to significant changes in the fracture morphology, and as a result of this, the fracture network lost some in situ microscopic properties (Zhuang et al., 2020).

In addition, the statistics and analysis provided by He et al. (2020) and Li et al. (2021) were mainly based on direct observation of the rock fracturing results under a microscope, so it was difficult to capture the geometric shape of fractures in the vertical direction. However, Jiang et al. (2019) and Yang et al. (2021) extracted the three-dimensional fracture network based on hydraulic fracturing of a rock. The extracted fracture network not only reflected the changes in fracture propagation in the different directions, but it could also be used to analyze the rock's seepage capacity after fracturing. Therefore, accurate and efficient extraction of the fracture network based on fracturing experiments is of great significance to the subsequent rational planning of oil and gas production (Gehne and Benson, 2019; Zhong et al., 2021).

In order to overcome the problem in which Jiang et al. (2019) and Yang et al. (2021) did not achieve in situ observations of the fracture network in their fracturing experiments, an online hydraulic fracturing CT scanning platform (HFCP) was developed in this study. We explored the influences of the confining pressure and injection rate on the growth of the hydraulic fracturing fracture network in homogeneous tight sandstone using an HFCP. In this study, it was directly demonstrated that an HFCP has the advantages of in situ high-resolution imaging, a short-time CT scanning, and efficiently accurate fracture network extraction. This paper is organized as follows. Section 2 introduces the CT system and power system of the HFCP. The tight sandstone hydraulic fracturing experiments and experimental procedure are presented in Section 3. The fracture extraction algorithm in the post-processing system is described in Section 4. The results of hydraulic fracturing experiments are discussed and analyzed in Section 5, and the conclusions are presented in Section 6.

2. Introduction to HFCP

The main components of the HFCP are shown in Fig. 1 and can be divided into a CT system and a power system. The CT system (green box in Fig. 1) includes a micro-CT and rock holder, which are the most important devices for rock fracturing experiments and CT scanning. The power system (gray box in Fig. 1) includes a pump unit, an injection container, and recovery equipment. It mainly provides loading to the rock during the experiment and collects residual fluid and rock debris after the experiment. The specially designed CT system and power system of the HFCP provide an adequate guarantee of in situ high-resolution CT imaging during the hydraulic fracturing of the rock sample.

2.1. CT system

Fig. 2 shows the micro-CT equipment used in the CT system, which is composed of a ray source, a pneumatic rotary table, and a receiving plate. The nanoVoxel-3000 micro-CT developed by Sanying Company with a maximum resolution of 7 μm is used in HFCP. The maximum power of the micro-CT ray source is 20 W, and multiple images can be combined automatically at the same scanning position to ensure that the fine fracture network developed in the rock can be identified. The installation relationship between micro-CT and holder is also shown in Fig. 2. After it is installed on the pneumatic rotary table, the holder is in a straight line with the ray source and receiving plate, thus meeting the rotation and alignment requirements for CT scanning. The resolution of CT imaging is controlled by adjusting the relative distance between the ray source, holder and receiving plate. The pipelines on the holder are divided into upper and lower parts and are semi-fixed to the wall of the

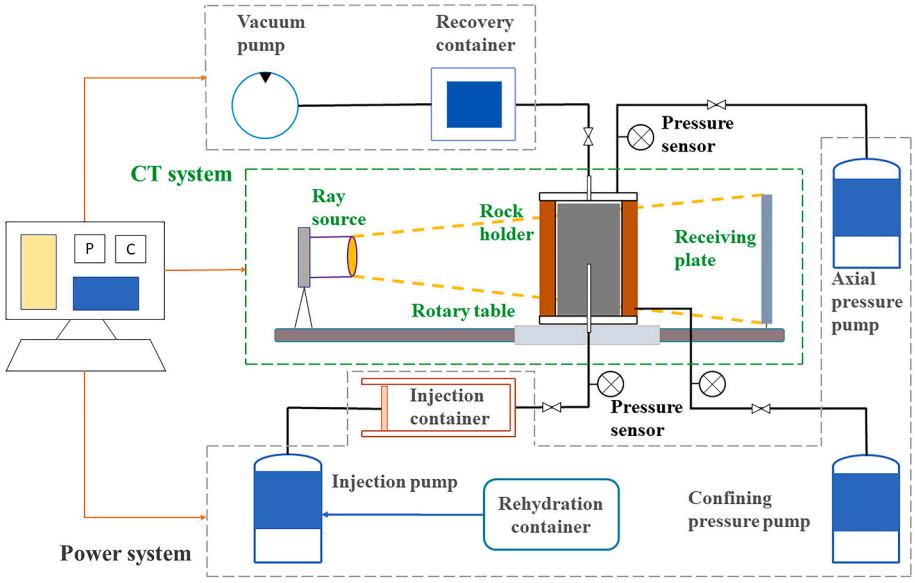

Fig. 1. Schematic of the HFCP. The green box is the CT system and the gray box is the power system. (For interpretation of the references to colour in this figure legend, the reader is referred to the Web version of this article.)

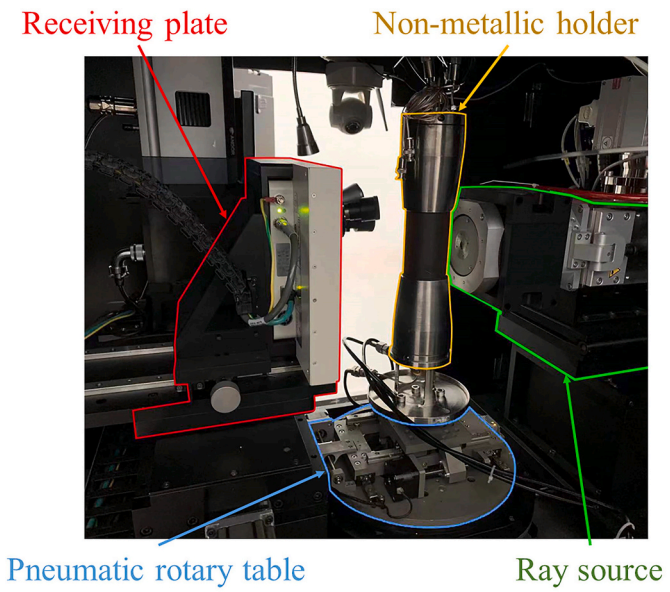

Fig. 2. The micro-CT used in CT system, and the installation of non-metallic holder inside the micro-CT.

CT. A suitable length should be reserved for the movable parts of pipelines, in order to avoid pulling the pipeline during the scanning rotation due to a pipeline too short or interference with the CT imaging due to a pipeline too long.

Al Shafloot et al. (2021) attempted to observe the in situ fracture networks while researching the propagation characteristics of fractures induced by $sc-CO_2$ and water in shale, but they failed because the time period of CT scanning was too long. Therefore, in order to ensure the effectiveness of in situ observations after rock fracturing, it is necessary to reduce the time period of the CT scanning as much as possible. In the HFCP, the time period of total scanning process is shortened by increasing the CT power and reducing the exposure time. In addition, the multiple lifting and rotation of the holder are avoided during the scanning of the hydraulic fractures by expanding the view of the ray source and setting an appropriate height for the installation of the holder. The main part of the fractures in the rock sample can be scanned in a single rotation based on the above measures. The time required to perform a single micro-CT scan is effectively controlled to less than 800 s, with a micro-CT vision of 1920 × 1920 × 1024 pixels and 1080 acquisition frames.

In order to attain the in situ observations, the holder in CT system was specially designed. Fig. 3 shows the connection of the pipeline to the holder and the internal details of the holder. Part of the holder is constructed of 10% carbon fiber reinforced polyimide that can withstand a confining pressure of 25 MPa, and this material wraps the rock horizontally. It is important to reduce the energy attenuation caused by the holder during the CT scanning of the rock while ensuring that the holder has sufficient strength, which improves the quality of scanning images of the rock and the fracture network. The top of the holder is connected to the recovery pipeline, axial pressure pipeline, and confining pressure pipeline, while the bottom of the holder is connected to the injection pipeline.

The specially designed fracturing plug and plunger in the CT system guarantee that the injected fracturing fluid is sealed into rock (Fig. 3). The installation methods of the rock, fracturing plug, fracturing plunger and holder are as follows. The top of the plug is inserted into the hole of the rock and is sealed with a rubber ring, and its side opening allows the injected fluid to load on the central hole of the rock. The bottom of the plug is connected to the top end of the plunger by an O-ring, and the bottom of the plunger is connected to the holder injection pipeline. The combination of the rock, plug and plunger are installed inside the holder using the tail threaded pipe. Compared with conventional glue sealing, the connection method of the HFCP has the advantages of convenient disassembly and assembly, and it can be installed and used between the rock and holder many times. The internal diameter of the fracturing plug and the hole through the fracturing plunger is 1.5 mm, and the specific overall dimension is determined based on the geometric dimensions of the rock and the holder. The fracturing plug and fracturing plunger are constructed of high-strength polyetheretherketone material, which can resist deformation a fluid pressure of 40 MPa.

To guarantee the effectiveness of the fracturing experiment, it is necessary to ensure the end face of rock is level and flat, and the direction of the blind hole at the center of rock is perpendicular. Thus, the

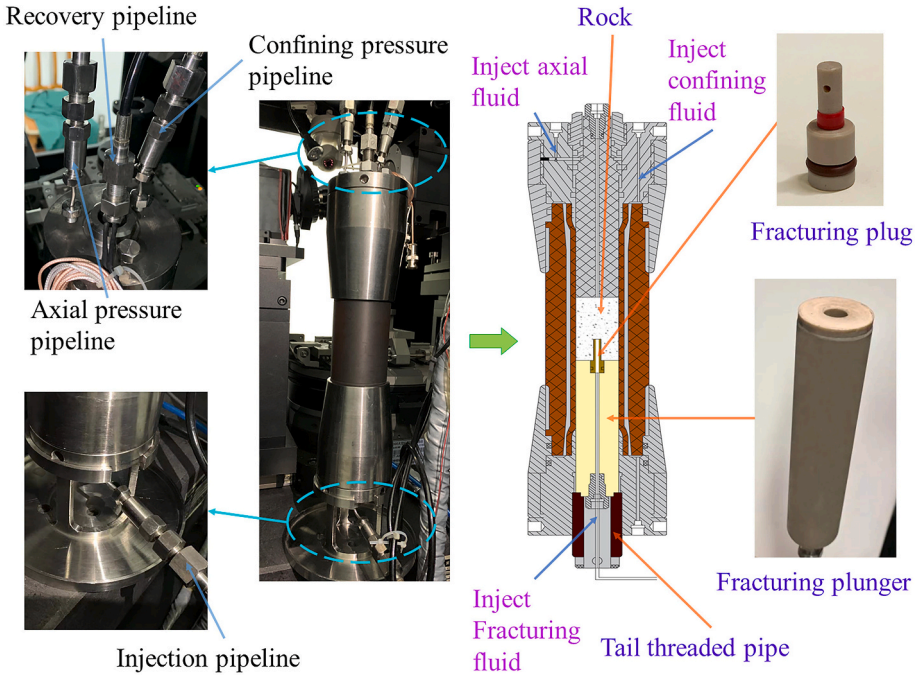

Fig. 3. The holder connected with pipelines and the internal details of the installation of rock, plug and plunger.

end face of the rock was cut using a wire cutting machine, and a twist drill was used to drill into the center of the end face of the rock using a bench drill before the experiment. The flatness of the end face of the rock should be $\pm 0.2mm$, and the direction between the blind hole and the vertical direction should be less than 2°.

2.2. Power system

The pump unit in the power system includes an injection pump, an axial pressure pump and a confining pressure pump, which provide power for the injection of the fluid and the application of anisotropic stress around the rock. The injection pump is shown in Fig. 4. Two operating modes can be set using the injection pump, that is, constant flow rate and constant pressure modes. In the constant flow rate mode, the maximum flow rate of the injection pump can be set to 30 ml/min. In the constant pressure mode, the maximum fluid pressure can be maintained at 50 MPa. In order to keep the pump from stopping during the fracturing experiment, the injection pump is required to have the ability to inject fluid constantly. In this experiment, a double-cylinder injection pump was used. When one of the cylinders is in use, the other cylinder can be refilled at the same time. The upper limits of the axial pressure pump and the confining pressure pump are both 25 MPa. Because the axial pressure and confining pressure are kept constant during the experiment, a single-cylinder pump can meet the experimental requirements.

The injection container of the power system is shown in Fig. 5. The inlet of the injection container is connected to the injection pump, and the outlet is connected to the injection pipeline outside of the holder. The injection fluid can be replaced and a propping agent can be added into the injection container. Then fracturing fluids of different types and viscosities can be injected into the rock using the injection pump. In addition, based on the different experimental conditions, multiple injection containers can be installed to realize a mixed injection of various types of fracturing fluids. The power system of the HFCP is controlled by pneumatic valves, and all of the pneumatic valves are powered by the same air compressor. Three pressure sensors are installed in the HFCP to monitor the injection fluid pressure, axial pressure and confining pressure in real time during the fracturing experiment. The pressure sensor can realize data collection at a 0.01 s interval.

The recovery equipment in the power system includes a recovery

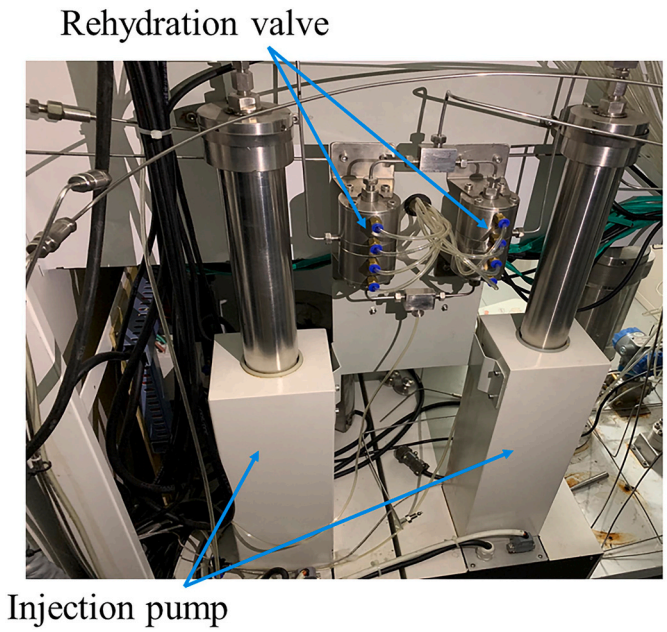

Fig. 4. The double-cylinder injection pump in the power system.

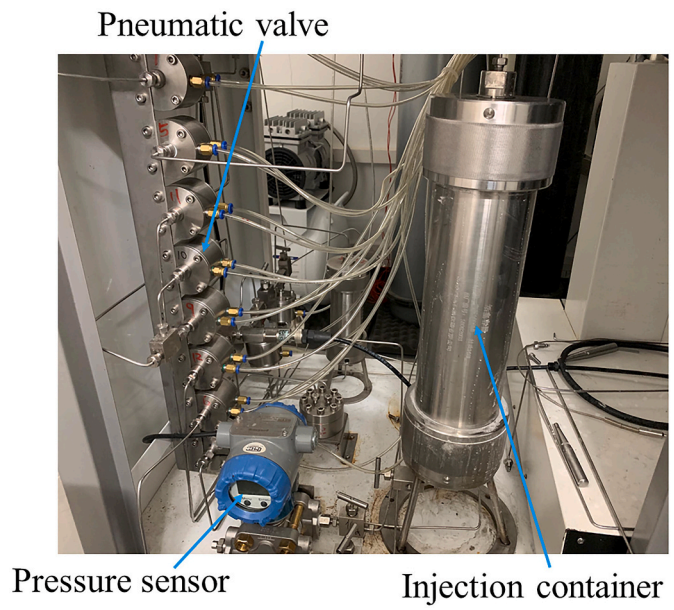

Fig. 5. The injection container in the power system.

container and a vacuum pump, which are mainly used to collect the residual fracturing fluid and the rock debris in the holder and pipeline after the fracturing experiment. An isolation cotton net is placed in the recovery container to separate the fracturing fluid and rock debris. The operating pressure of the vacuum pump is set as 5×10^{-5}Pa (absolute pressure) to avoid the impact of an excessive recovery flow rate on the pipeline.

In summary, the CT system and power system in HFCP meet the requirements of short-term high-resolution CT imaging while ensuring that the equipment can withstand changes in the fluid pressure. Therefore, the HFCP can scan the rock serval times without disassembling the holder during the fracturing experiment, achieving in situ high-resolution observation under fracturing conditions.

3. Experiments

The hydraulic fracturing experiments were carried out using the HFCP. In this study, samples from the tight sandstone outcrops in the Yanchang area of Xi'an were used. The samples had a porosity of 2.6%, a permeability of 0.3 mD, and a density of 2.63 g/cm^3. The external structure of the cut cylindrical rock samples is shown in Fig. 6a. The diameter of the circular end face of the rock was 25 mm and the total height was 30 mm. A blind hole (4 mm in diameter and 10 mm deep) was drilled in the center of the end face of the rock. The basic mechanical properties of the tight sandstone samples are presented in Table 1. In addition, a polarized light microscope was used to observe multiple sets of cast thin sections of the tight sandstone (Fig. 6b). It was found that the rock is mainly composed of brittle minerals, and the brittle mineral interface is connected by a small amount of clay minerals. The three main minerals in the rocks were quartz, feldspar, and pyrite. Table 2 presents the statistics of the main mineral composition, content, and particle size range of the rock samples. Based on the cast thin section observations, it was found that the minerals were evenly distributed in the rock and have a favorable homogeneity overall.

We conducted fracturing experiments on rock samples under different constant flow rates and two confining pressures (1 MPa and 5 MPa). The experiments were carried out using the fracturing parameters in Table 3. The injection fluid pressure recording interval of the sensor was 0.05 s, and clean water was selected as the fracturing fluid added to the injection container. During the experiments, the voltage of the micro-CT was 175 kV, the current was 0.11 mA, and the number of

Fig. 6. (a) Tight sandstone sample with a blind hole in the center and (b) photograph of a cast thin section of the rock sample.

Table 1
Basic mechanical properties of the tight sandstone.

Tensile strength (MPa)	Uniaxial compressive strength (MPa)	Young's modulus (GPa)	Poisson's ratio
4.18	63.21	10.12	0.21

Table 2
The main mineral composition, contents and particle size range of the tight sandstone.

Mineral	Mineral content (%)	Mineral size range (mm)
Quartz	71	0.2–0.6
Feldspar	24	0.2–0.6
Pyrite	5	0.3–2.5

Table 3
Fracturing parameters used in experiments on tight sandstone.

Experimental parameters	Value
Injection rate (cm^3/ min)	2, 3, 4
Confining pressure (*MPa*)	1, 5
Axial pressure (*MPa*)	5
Dynamic viscosity ($mPa \cdot s$)	1

merged images at the same position was 2. The single scan time was 726 s, and the field of vision of the micro-CT was 1920 × 1920 × 1080 pixels. The resolution of the rock scan image was 14.95 μm, and the number of acquisition frames was 1080.

For the fracturing experiments carried out using the HFCP, we established a corresponding experimental procedure and attained in situ high-resolution observations. In the preparation stage of experiment, the rock was cut and drilled, and the holder connected to the pipeline was fixed to the pneumatic rotary table of Micro-CT. The main flow of the hydraulic fracturing experiment using the HFCP was as follows.

(1) The axial pressure and confining pressure were applied. The geostress around the rock was simulated and the rock was held in the center of the holder.
(2) An initial CT scan of the rock was obtained before the fracturing. The micro-CT reconstructed images obtained before and after the fracturing were compared using grayscale calibration to determine the threshold range of the fracture network after the rock fracturing. It was observed whether there were obvious fractures or pores before the fracturing to assess the influence of the initial defects on the growth of the fracture network.
(3) The switching valves of the injection container and the injection pipeline of the holder were opened. It was ensured that the injection pipeline was filled with the fracturing fluid and the air was removed from the pipeline.
(4) The switching valves of the injection pipeline for injecting fluid into the rock were closed, and the recording module that monitors the injection fluid pressure in real time was opened. Within a certain period of time, if the fluid pressure did not rise or remained the same, then the seepage in the rock caused fracturing of the rock to fail. It was necessary to shut down the injection pump and stop the fracturing experiment. If the fluid pressure increased steadily, then the fracturing experiment was continued.
(5) When the fluid pressure dropped significantly in a short time, it was necessary to promptly conduct in situ CT scanning of the rock. The pressure curve of the rock fracturing process is shown in Fig. 7, and it can usually be divided into three stages: loading, fracturing, and post-fracturing. The breakdown pressure between the loading stage and the fracturing stage is the highest point on the fluid pressure curve. One or more macroscopic through fractures have been generated when the fluid pressure is loaded to the breakdown pressure, thus leading to a rapid decrease in the fluid pressure. In the post-fracturing stage, the main body of the fracture surfaces becomes stable, and the continuous injection of fluid causes the fluid pressure in the central hole of the rock to be slightly higher than the confining pressure. The in situ micro-CT scanning was carried out immediately in the post-fracturing stage, and the micro-CT images were used to preliminarily determine the fracture morphology.
(6) The injection pump was turned off and the vacuum pump was turned on. The residual liquid and rock debris in the injection pipeline were cleaned out.
(7) The axial pressure and confining pressure around the rock were removed. The hydraulic fracturing experiment was ended, the device was disassembled, and the rock was removed from the holder.

The experimental procedure of hydraulic fracturing experiments conducted using the HFCP is shown in Fig. 8.

4. Post-processing system

The accurate extraction of the fracture network in rock was realized using the post-processing system of HFCP and the results of the in situ high-resolution micro-CT scanning. The post-processing system mainly includes four parts: rock reconstruction, grayscale calibration, threshold segmentation, and efficient extraction of the fracture network. The process of extracting the fracture network based on the micro-CT data obtained before and after fracturing is shown in Fig. 9.

First, the micro-CT scanning data obtained before and after fracturing were used for the rock reconstruction (Fig. 9a). The fracturing plug and non-metallic holder can be separated in the rock image during

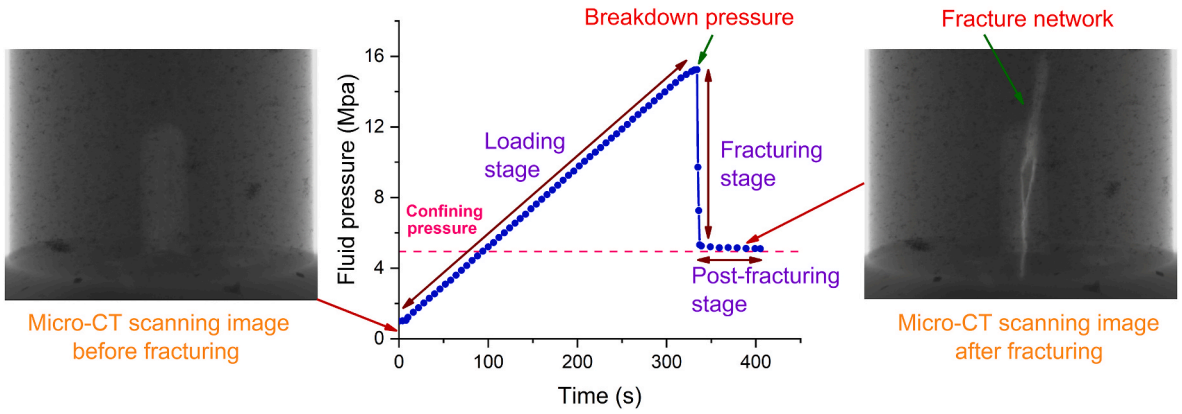

Fig. 7. During the fracturing experiment, the curve of change in the fluid pressure with time and the three stages of the fracturing process.

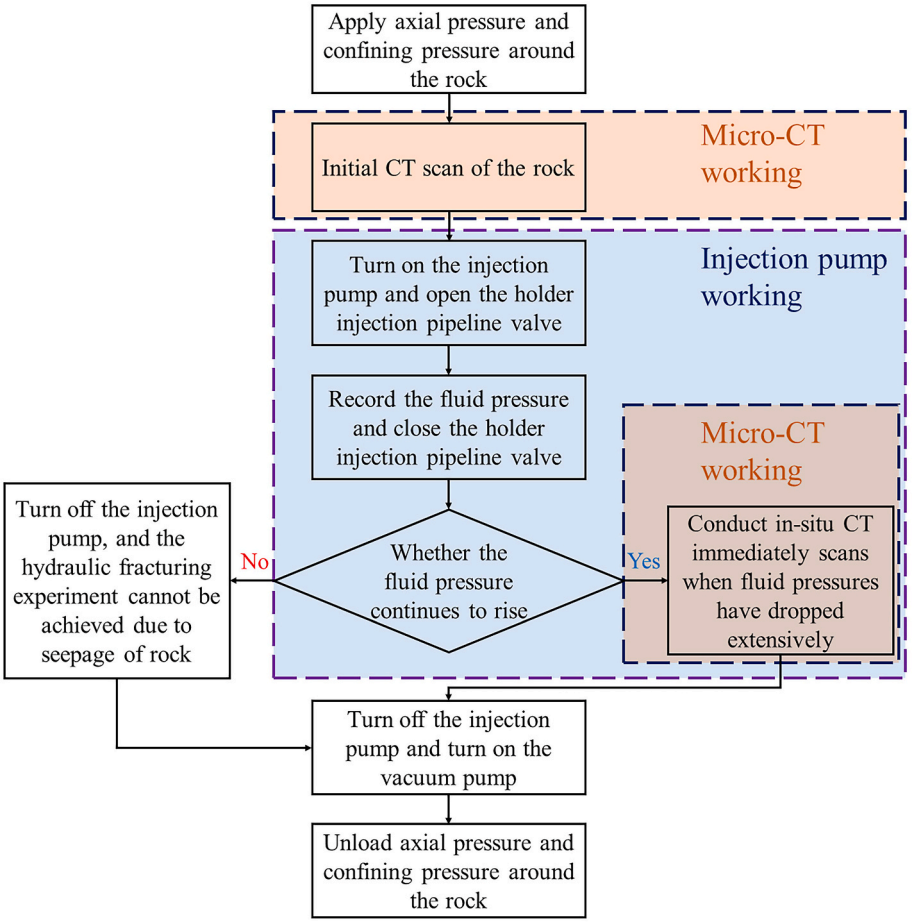

Fig. 8. Flow chart of experimental procedure using the HFCP.

the rock reconstruction stage due to the obvious differences in their densities. Only the rock and fracture data were retained and the reconstructed image was stored as 16 bits.

Then, grayscale calibration was carried out to construct a grayscale image (Fig. 9b). Grayscale calibration eliminates the grayscale difference between the scanned images before and after the rock fracturing due to fluid immersion. The calibration process was based on the landmark minerals at the same height section in the rock before and after fracturing to unify the grayscale of the scanning images. Based on the grayscale images of the rock before and after fracturing, the gray attenuation area of the fracture body and boundary were accurately delineated, and thus, the threshold range of the fracture could be determined.

Furthermore, threshold segmentation was conducted on the fractures in the rock (Fig. 9c). In order to accurately identify the fracture network formed in the fracturing experiment, the initial defects coincident with the fracture surfaces within the threshold range were marked or removed by comparing the threshold segmentation results before and after fracturing. In addition, to avoid isolated micro-defects within the threshold range of the rock being extracted, during the threshold segmentation, small-size defects were filtered based on pixel volume quantity judgment.

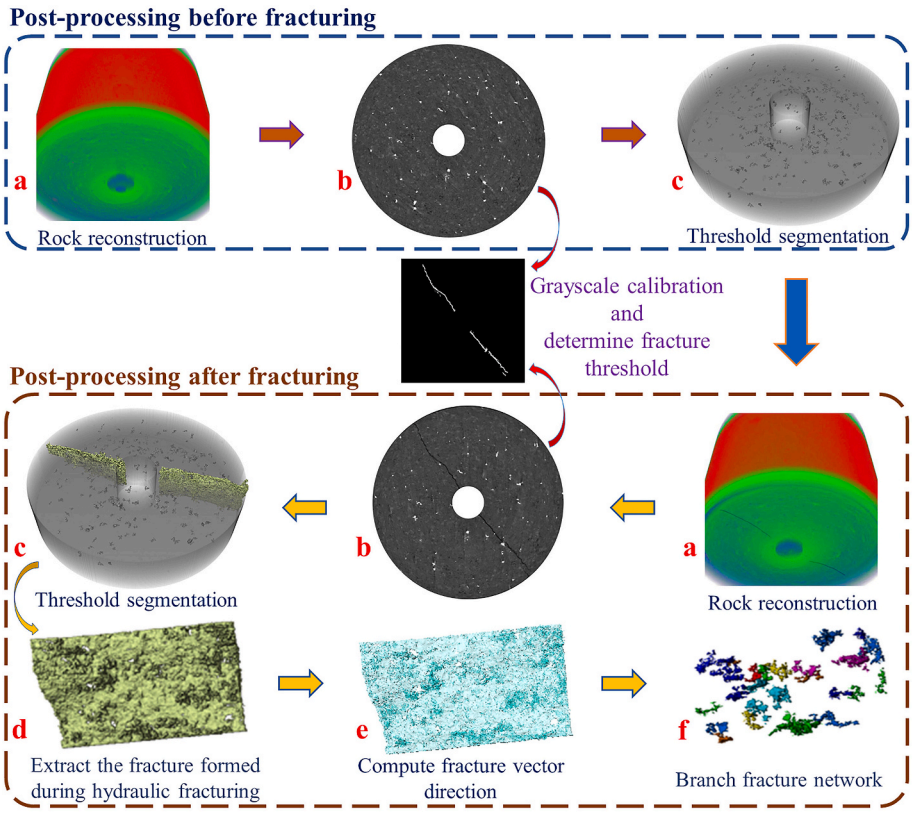

Fig. 9. The rock reconstruction, grayscale calibration, threshold segmentation, and fracture network extraction steps of the post-processing. (a) First, the rock image is reconstructed based on the micro-CT results obtained before and after fracturing. (b) Then, the two reconstructed grayscale rock images are calibrated, and the threshold of the fracture is determined. (c) Next, the threshold of the rock and fractures are segmented, and the original defects around the fractures are marked or removed. (d, e, f) Finally, the in situ fracture surfaces and branch fractures are extracted.

Finally, the fracture surfaces were efficiently extracted using the medial axis-maximal ball (AB) algorithm and fracture morphology, and the branch fractures on the fracture surfaces were identified by the vector direction (Fig. 9d, e, f). In this study, we defined the fractures that extended from the central hole to the rock wall as the main fractures. Branch fractures were defined as fractures that extended from the main fractures and for which the vector between the bottom and the tip was significantly different from the vector of the main fractures. In the post-processing system, the AB algorithm proposed by Yi et al. (2017) was used to extract a physically realistic pore and fracture network. The center axis of the pore and fracture network after fracturing was used to guide the construction of the maximal-balls-like skeleton of the fractures. The fracture network extracted represents of the fracture space in the sense of topology and morphology and is also a good tool for accurately predicting the transport properties. The balls in the skeleton were then connected to form a fracture network in order to identify the bottom and tip of the fracture. The different vectors of the fractures were finally determined based on the maximal-balls-like skeleton, and the main fracture surfaces were distinguished from the branch fractures.

5. Results and discussion

In this section, we select the results of six representative experiments for comparison based on the fracturing experiments described in Section 3. The variations in the injection fluid pressure and fracture network with confining pressure and injection rate during fracturing are discussed.

5.1. Variations in injection fluid pressure

After the injection fluid pressure is loaded to 1 MPa, the curves of pressure with time for all of the rock samples are shown in Fig. 10. Due to the low permeability of the rock samples used in the fracturing experiments, the slope of the curve remained stable during the loading

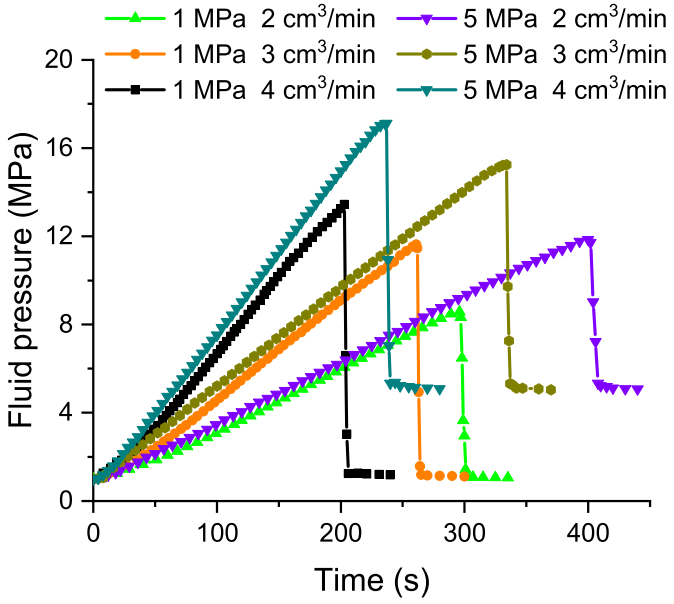

Fig. 10. Influences of confining pressure and injection rate on fluid pressure during the fracturing experiment.

stage, and there was no obvious pressure initiation point. Fig. 10 shows that when the loading time was the same, the fluid pressure increased with the rise of the confining pressure, because a high confining pressure caused the closure of some micro-defects in the rock sample and reduced the fluid seepage speed in the rock.

However, Fig. 10 also shows that the increase in injection rate increased the slope of the fluid pressure curve. The higher injection rate accelerated the compression rate of fluid in the rock's central hole and in

the injection pipeline, so the slope of the pressure curve increased at the same time. Because a stable fracture surface had already formed in the fracturing stage, the continuous injection of fluid in the post-fracturing stage maintained the fluid pressure similar to the confining pressure.

The variations in the breakdown pressure of the injection fluid with the injection rate and confining pressure are shown in Fig. 11. As the confining pressure increased, the interaction between mineral particles became stronger, and thus, a higher breakdown pressure was needed to form a fracture network in the rock. As the injection rate increased, the breakdown pressure of the injection fluid increased under the two different confining pressures. Based on low-permeability and low-porosity rocks, Garagash and Detournay (1996, 1997) theoretically explained the phenomenon that an increase in the injection rate caused an increase in the breakdown pressure. They established the relationship between the dimensionless breakdown pressure and the pressurization rate considering one-dimensional lubrication flow in the fracture coupled with the non-local elastic response of the fracture and other conditions. They proved that under the assumption of fluid incompressibility, the breakdown pressure will increase infinitely as the injection rate increase. Fig. 11 also shows that the increase in the amplitude of breakdown pressure decreased with increasing injection rate under the different confining pressures.

5.2. Variations in the fracture network

The micro-CT data obtained before and after the rock fracturing were subjected to post-processing. The grayscale threshold range of fractures was determined to be 3245–12435. The threshold segmentation results of the six rock samples before fracturing show that the interiors of all of the rock samples were intact, and no defects were caused during the rock preparation. In this study, the analysis zone consisted of 400 cross sections, which were continuously intercepted from the end face by the blind hole in the center of the rock. Focusing on the analysis zone of each rock sample, the influence of the injection rate on the fracture network's morphological and quantitative characteristics under the two confining pressures was analyzed.

5.2.1. Morphological characteristics of the fracture network

Fig. 12 show grayscale images of the rock after fracturing, the threshold segmentation fracture network, and the variations in the extracted single-wing fracture surface and branch fractures with

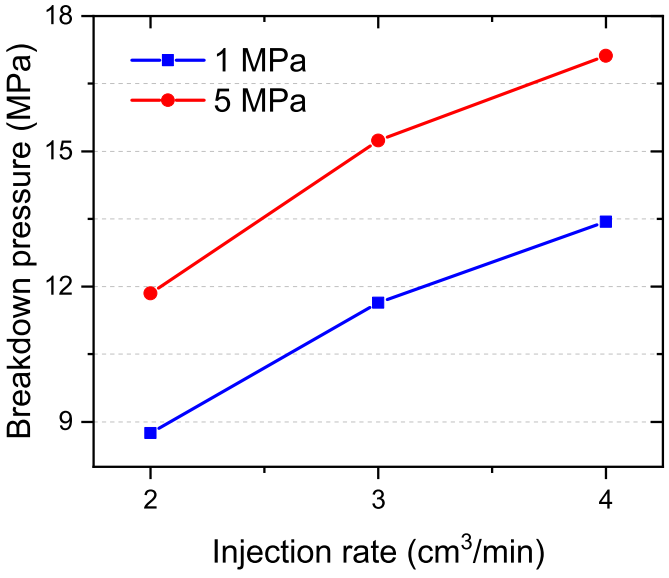

Fig. 11. Influence of injection rate on the breakdown pressure under different confining pressures.

injection rate under the two different confining pressures. By comparing the grayscale images in Fig. 12, it was found that there were always two main fractures around the central hole in the rock sample, and they were distributed symmetrically around the midpoint of the rock. This is the same as the number and distribution of the main fractures obtained by Kumari et al. (2018), Lin et al. (2019), and Zhang et al. (2019) through hydraulic fracturing experiments on cylindrical rock samples. The threshold segmentation shows that the direction of the fracture network in the rock sample was hardly affected by the change in the height.

Through comparison of all of the experimental rock samples, it was found that the main fractures formed in rock tended to be more complete as the injection rate increased under both of the confining pressures. This occurred because after the breakdown pressure increased as the injection rate increased under the same confining pressure. As a result, the rock released more strain energy during fracturing, which was more conducive to the formation of a complete main fracture surface in the rock. However, through further comparison of the branch fracture data, it was found that when the confining pressure was 1 MPa, the volume of the branch fracture network decreased with increasing injection rate, while the opposite relationship occurred when the confining pressure was 5 MPa. We explain the most likely reasons for the different trends of the branch fracture volume in the next section, based on the quantitative statistics of the geometric characteristics of the fracture network.

5.2.2. Quantitative characteristics of the fracture network

Based on the fracture network data obtained from the experiments, the hydraulic fracturing effect was evaluated quantitatively. Regarding the statistics of geometric parameters of hydraulic fracture network, the aperture and complexity of fracture network are very important. Increasing the aperture and complexity of the fracture network can reduce the resistance of oil and gas flow to the wellbore and increase the seepage area between the fracture and the reservoir, thus significantly improving the oil and gas production efficiency (Li and Einstein, 2019; Gou et al., 2021). In this study, the average fracture aperture and branch fracture volume fraction were used as quantitative statistical parameters to reflect the aperture and complexity of the fracture network.

The average value of the fracture aperture of 400 sections obtained in the experiment was defined as the average fracture aperture. The ratio of the branch fracture volume to total fracture volume is defined as the branch fracture volume fraction. Under the two confining pressures, the statistical results of the average fracture aperture and the branch fracture volume fraction in the fracture network are shown in Fig. 13. According to Fig. 13, for the specific fracturing parameters and rock types, the continuous increase in the injection rate under the same confining pressure improved the average fracture aperture. However, as the confining pressure increased, the influence of the injection rate on the average fracture aperture weakened. The volume fraction of the branch fractures exhibited different characteristics with increasing injection rate under the different confining pressures. Based on the research conducted by Renshaw and Pollard (1995) on the mechanism of compressional crossing, the theoretical derivation and experimental results reported by Li et al. (2021) on the promotion of branching of hydraulic fractures, and the results of this study, we speculate that the most likely reasons for the influences of confining pressure and injection rate on the branch fractures are as follows. When the confining pressure is low, the formation rate of the fracture network increases with increasing injection rate, resulting in the fracture propagation rate being greater than the injection rate of the fluid. As a result, the fluid does not produce enough pore pressure on both sides of the main fracture to form branch fractures, and thus, the volume of the branch fractures decreases. When the confining pressure is high, the formation rate of the main fracture does not increase significantly at the current injection rate, and the fracture interface is always close to the fluid level. Increasing the injection rate causes an increase in the pore pressure in the weak structure of rock matrix, which provides a tensile opening force for the formation of branch fractures, leading to a gradual increase in the

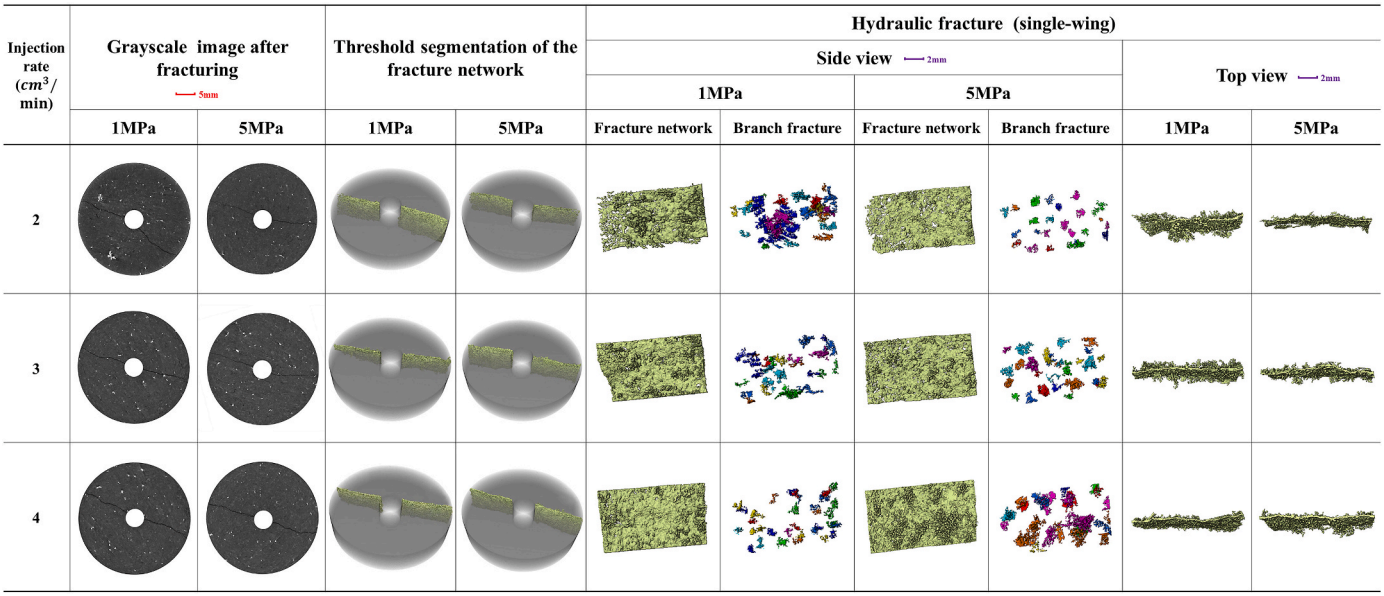

Fig. 12. Grayscale images, threshold segmentation fracture of the network, and extracted single-wing fractures and branch fractures under different injection rates at a confining pressure of 1 MPa and 5 MPa.

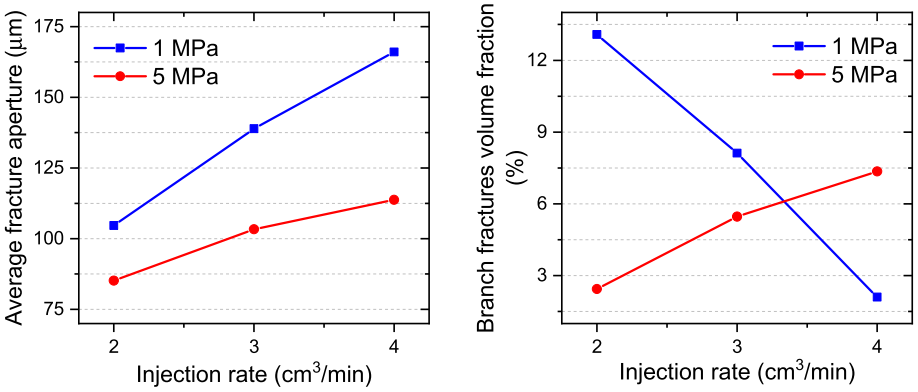

Fig. 13. Variations in the average fracture aperture and branch fracture volume fraction with injection rate under different confining pressures.

branch fracture volume. Based on the above statistics and the morphology of the fracture network, we conclude that under the same confining pressure, increasing the injection rate can improve the average aperture of fractures; however, the relationship between the injection rate and the complexity of fracture network is not monotonous.

Other experiments have also been conducted under different stress loading conditions, and they statistically summarized the influence of sole controlling the injection rate on the growth of fracture networks in tight rocks. When using a high-speed camera to photograph the fracturing experiment conducted on the Opalinus shale and Barre granite, Li and Einstein. (2019) discovered that as the injection rate increases the number of branch fractures decreased. Cheng et al. (2020) reported the statistics of the AE activity and fractures in Songliao granite during the fracturing process and found that a more complex fracture network more easily forms as the injection rate increases. These experimental results provide strong evidence that increasing the injection rate will have different effects on the complexity of the fractures under different confining pressures. Furthermore, fracturing experiments using an HFCP can be conducted to extract the in situ three-dimensional fracturing network. This is of great significance for subsequent research on the impact of fracturing on the rock mechanical behavior and seepage properties using digital cores (Ji et al., 2019; Hou et al., 2021).

6. Conclusions

In order to achieve high-resolution in situ observation of a rock fracture network, an online hydraulic fracturing CT scanning platform (HFCP) was developed in this study. The HFCP is composed of a CT system for in situ high-resolution imaging, a power system with continuously changeable fluid pressure, and a post-processing system for efficient extraction of the fracture network. In addition, hydraulic fracturing experiments on tight sandstone were carried out using the HFCP to explore the influences of the confining pressure and injection rate on the fluid pressure and the characteristics of fracture network. Furthermore, the HFCP provides a new in situ high-resolution method for studying the mechanism of hydraulic fracturing of rocks. The specific conclusions drawn from the results of this study are as follows.

(1) The major scanning parameters, fracturing plug, and plunger in the CT system were specially designed, which not only shortened the scanning time but also fundamentally solved the feasibility problem of in situ high-resolution observation during fracturing experiments.
(2) A special experimental procedure was developed for the HFCP, and the specific steps of micro-CT scanning before and after

fracturing were defined. Thereby, in situ high-resolution observation of the fracturing network in a rock was achieved.

(3) The grayscale calibration of the reconstructed images was carried out based on the in situ high-resolution observations, ensuring the accuracy of the fracture threshold segmentation. Furthermore, the efficient AB algorithm was used to achieve accurately extraction of the in situ fracture network.

(4) The HFCP was used to conduct fracturing experiments on tight sandstone with confining pressures of 1 MPa and 5 MPa and injection rates of 2, 3, and 4 cm^3/min. The statistics of the experimental results revealed that increasing the injection rate under the two confining pressures increased the breakdown pressure and the average fracture aperture. However, the variations in the volume fraction of the branch fractures differed under the two confining pressures. It decreased with increasing injection rate under a confining pressure of 1 MPa, while it increased with the increasing injection rate under a confining pressure of 5 MPa.

Because the rock sample is always in the holder during the fracturing experiment and micro-CT scanning, the morphology and quantitative characteristics of the in situ fracturing network obtained using an HFCP are close to the micro-fracture network generated during downhole fracturing. However, at present, the direct guiding ability of an HFCP for on-site hydraulic fracturing is limited because the size of the rock sample and the confining pressure in all directions cannot be differentiated. In a future study, we will combine the experimental results and numerical simulations through non-dimensional analysis in order to expand the research scope and make it consistent with actual formation loading, thereby providing guidance for field fracturing construction.

Author statement

Siping Zheng: Writing, Visualization, Methodology. **Mian Lin**: Programming, Revise. **Wenbin Jiang**: Experiments. **Xin Qiu**: Supervision, Review & Editing. **Zhuo Chen**: Review & Editing.

Declaration of competing interest

The authors declare that they have no known competing financial interests or personal relationships that could have appeared to influence the work reported in this paper.

Acknowledgements

The authors gratefully acknowledge the support provided by the Strategic Priority Research Program of the Chinese Academy of Sciences (Grant No. XDA14010304), the National Natural Science Foundation of China (Grant No. 42030808), the National Natural Science Foundation of China (Grant No. 41690132) and the National Natural Science Foundation of China (Grant No. 41872163).

References

Al Shafloot, T., Kim, T.W., Kovscek, A.R., 2021. Investigating fracture propagation characteristics in shale using sc-CO2 and water with the aid of X-ray Computed Tomography. J. Nat. Gas Sci. Eng. 92 https://doi.org/10.1016/j.jngse.2020.103736.

Chen, J., Li, X., Cao, H., Huang, L., 2020. Experimental investigation of the influence of pulsating hydraulic fracturing on pre-existing fractures propagation in coal. J. Petrol. Sci. Eng. 189 https://doi.org/10.1016/j.petrol.2020.107040.

Cheng, Y., et al., 2020. Experimental and numerical studies on hydraulic fracturing characteristics with different injection flow rates in granite geothermal reservoir. Energy Sci. Eng. 9 (1), 142–168. https://doi.org/10.1002/ese3.816.

Deng, B., et al., 2018. Feature of fractures induced by hydrofracturing treatment using water and L-CO2 as fracturing fluids in laboratory experiments. Fuel 226, 35–46. https://doi.org/10.1016/j.fuel.2018.03.162.

Du, Y., et al., 2020. Microfluidic diagnostics of the impact of local microfracture connectivity on hydrocarbon recovery following water injection. Water Resour. Res. 56 (7) https://doi.org/10.1029/2019WR026944.

Feng, R., Zhang, Y., Rezagholilou, A., Roshan, H., Sarmadivaleh, M., 2019. Brittleness index: from conventional to hydraulic fracturing energy model. Rock Mech. Rock Eng. 53 (2), 739–753. https://doi.org/10.1007/s00603-019-01942-1.

Garagash, D., Detournay, E., 1996. Influence of pressurization rate on bolehore breakdown pressure in impermeable rocks. In: 2nd North American Mechanics Symposium. OnePetro.

Garagash, D., Detournay, E., 1997. An analysis of the pressurization rate on the borehole breakdown pressure. Int. J. Solid Struct. 34 (24), 3099–3118. https://doi.org/10.1016/S0020-7683(96)00174-6.

Gehne, S., Benson, P.M., 2019. Permeability enhancement through hydraulic fracturing: laboratory measurements combining a 3D printed jacket and pore fluid overpressure. Sci. Rep. 9 (1), 12573 https://doi.org/10.1038/s41598-019-49093-1.

Gou, B., et al., 2021a. Effect of different types of stimulation fluids on fracture propagation behavior in naturally fractured carbonate rock through CT scan. J. Petrol. Sci. Eng. 201, 108529 https://doi.org/10.1016/j.petrol.2021.108529.

Gou, Q., Xu, S., Hao, F., Shu, Z., Zhang, Z., 2021b. Making sense of micro-fractures to the Longmaxi shale reservoir quality in the Jiaoshiba area, Sichuan Basin, China: implications for the accumulation of shale gas. J. Nat. Gas Sci. Eng. 94 https://doi.org/10.1016/j.jngse.2021.104107.

Guo, T., et al., 2021. Physical simulation of hydraulic fracturing of large-sized tight sandstone outcrops. SPE J. 26 (1), 372–393. https://doi.org/10.2118/204210-PA.

Hampton, J., Gutierrez, M., Matzar, L., Hu, D., Frash, L., 2018. Acoustic emission characterization of microcracking in laboratory-scale hydraulic fracturing tests. J. Rock Mech. Geotech. Eng. 10 (5), 805–817. https://doi.org/10.1016/j.jrmge.2018.03.007.

He, J., Li, X., Yin, C., Zhang, Y., Lin, C., 2020. Propagation and characterization of the micro cracks induced by hydraulic fracturing in shale. Energy 191. https://doi.org/10.1016/j.energy.2019.116449.

Hou, P., et al., 2021. 3D multi-scale reconstruction of fractured shale and influence of fracture morphology on shale gas flow. Nat. Resour. Res. 30 (3), 2463–2481. https://doi.org/10.1007/s11053-021-09861-1.

Ji, L., et al., 2019. Investigation into the apparent permeability and gas-bearing property in typical organic pores in shale rocks. Mar. Petrol. Geol. 110, 871–885. https://doi.org/10.1016/j.marpetgeo.2019.08.030.

Jiang, C., et al., 2019. CT-based 3D reconstruction of the geometry and propagation of hydraulic fracturing in shale. J. Petrol. Sci. Eng. 179, 899–911. https://doi.org/10.1016/j.petrol.2019.04.103.

Kumari, W.G.P., et al., 2018. Hydraulic fracturing under high temperature and pressure conditions with micro CT applications: geothermal energy from hot dry rocks. Fuel 230, 138–154. https://doi.org/10.1016/j.fuel.2018.05.040.

Li, B.Q., Einstein, H.H., 2019. Direct and microseismic observations of hydraulic fracturing in Barre granite and Opalinus clayshale. J. Geophys. Res. Solid Earth 124, 11900–11916. https://doi.org/10.1029/2019JB018376.

Li, H., Shi, Y., 2021. Triaxial experimental investigation into the characteristics of acid-etched fractures and acid fracturing. J. Petrol. Sci. Eng. 202, 108431 https://doi.org/10.1016/j.petrol.2021.108431.

Li, N., et al., 2021a. Effect of thermal shock on laboratory hydraulic fracturing in Laizhou granite: an experimental study. Eng. Fract. Mech. 248 https://doi.org/10.1016/j.engfracmech.2021.107741.

Li, W., et al., 2021b. Injection parameters that promote branching of hydraulic cracks. Geophys. Res. Lett. 48 (12) https://doi.org/10.1029/2021GL093321.

Li, Y., Liu, W., Yan, W., Deng, J., Li, H., 2019. Mechanism of casing failure during hydraulic fracturing: lessons learned from a tight-oil reservoir in China. Eng. Fail. Anal. 98, 58–71. https://doi.org/10.1016/j.engfailanal.2019.01.074.

Lin, C., He, J., Li, X., Wan, X., Zheng, B., 2016. An experimental investigation into the effects of the anisotropy of shale on hydraulic fracture propagation. Rock Mech. Rock Eng. 50 (3), 543–554. https://doi.org/10.1007/s00603-016-1136-4.

Lin, C., Mao, J., He, J., Li, X., Zhao, J., 2019. Propagation characteristics and aperture evolution of hydraulic fractures in heterogeneous granite cores. Arabian J. Geosci. 12 (22) https://doi.org/10.1007/s12517-019-4887-x.

Qian, Y., et al., 2020. Advances in laboratory-scale hydraulic fracturing experiments. Adv. Civ. Eng. 1–18. https://doi.org/10.1155/2020/1386581, 2020.

Renshaw, C.E., Pollard, D.D., 1995. An experimentally verified criterion for propagation across unbounded frictional interfaces in brittle, linear elastic materials. Int. J. Rock Mech. Min. Sci. Geomech. Abstr. 32 (3), 237–249. https://doi.org/10.1016/0148-9062(94)00037-4.

Roth, S.-N., Léger, P., Soulaïmani, A., 2020. Strongly coupled XFEM formulation for non-planar three-dimensional simulation of hydraulic fracturing with emphasis on concrete dams. Comput. Methods Appl. Mech. Eng. 363 https://doi.org/10.1016/j.cma.2020.112899.

Wu, Z., Cui, C., Jia, P., Wang, Z., Sui, Y., 2021. Advances and challenges in hydraulic fracturing of tight reservoirs: a critical review. Energy Geoscience. https://doi.org/10.1016/j.engeos.2021.08.002. In press.

Yang, B., et al., 2021. Digital quantification of fracture in full-scale rock using micro-CT images: a fracturing experiment with N2 and CO2. J. Petrol. Sci. Eng. 196 https://doi.org/10.1016/j.petrol.2020.107682.

Yi, Z., et al., 2017. Pore network extraction from pore space images of various porous media system. Water Resour. Res. 53 (4), 3424–3445. https://doi.org/10.1002/2016WR019272.

Zhang, R., Hou, B., Han, H., Fan, M., Chen, M., 2019a. Experimental investigation on fracture morphology in laminated shale formation by hydraulic fracturing. J. Petrol. Sci. Eng. 177, 442–451. https://doi.org/10.1016/j.petrol.2019.02.056.

Zhang, Y., et al., 2019b. An experimental investigation into the characteristics of hydraulic fracturing and fracture permeability after hydraulic fracturing in granite. Renew. Energy 140, 615–624. https://doi.org/10.1016/j.renene.2019.03.096.

Zhong, X., et al., 2021. Fracture network stimulation effect on hydrate development by depressurization combined with thermal stimulation using injection-production well patterns. Energy 228. https://doi.org/10.1016/j.energy.2021.120601.

Zhou, F., et al., 2019. Integrated hydraulic fracturing techniques to enhance oil recovery from tight rocks. Petrol. Explor. Dev. 46 (5), 1065–1072. https://doi.org/10.1016/S1876-3804(19)60263-6.

Zhuang, L., Kim, K.Y., Diaz, M., Yeom, S., 2020. Evaluation of water saturation effect on mechanical properties and hydraulic fracturing behavior of granite. Int. J. Rock Mech. Min. Sci. 130 https://doi.org/10.1016/j.ijrmms.2020.104321.